Electric and magnetic losses modeled by a stable hybrid with explicit–implicit time-stepping for Maxwell's equations

Tomas Halleröd *, Thomas Rylander

Department of Signals and Systems, Chalmers University of Technology, S-412 96 Göteborg, Sweden

Abstract

A stable hybridization of the finite-element method (FEM) and the finite-difference time-domain (FDTD) scheme for Maxwell's equations with electric and magnetic losses is presented for two-dimensional problems. The hybrid method combines the flexibility of the FEM with the efficiency of the FDTD scheme and it is based directly on Ampère's and Faraday's law. The electric and magnetic losses can be treated implicitly by the FEM on an unstructured mesh, which allows for local mesh refinement in order to resolve rapid variations in the material parameters and/or the electromagnetic field. It is also feasible to handle larger homogeneous regions with losses by the explicit FDTD scheme connected to an implicitly time-stepped and lossy FEM region. The hybrid method shows second-order convergence for smooth scatterers. The bistatic radar cross section (RCS) for a circular metal cylinder with a lossy coating converges to the analytical solution and an accuracy of 2% is achieved for about 20 points per wavelength. The monostatic RCS for an airfoil that features sharp corners yields a lower order of convergence and it is found to agree well with what can be expected for singular fields at the sharp corners. A careful convergence study with resolutions from 20 to 140 points per wavelength provides accurate extrapolated results for this non-trivial test case, which makes it possible to use as a reference problem for scattering codes that model both electric and magnetic losses.
© 2008 Elsevier Inc. All rights reserved.

1. Introduction

Radar absorbing materials (RAM) with electric and magnetic losses are important for the reduction of the radar cross section (RCS) in stealth applications [1]. Optimized designs may involve geometries with sharp

---

* Corresponding author. Tel.: +46 31 772 1578; fax: +46 31 772 1748.
  E-mail addresses: tomas.hallerod@chalmers.se (T. Halleröd), rylander@chalmers.se (T. Rylander).

edges and inhomogeneous materials. Thus, *local* mesh refinement may be necessary to resolve rapid variations in the electromagnetic field and/or the material parameters.

Ampère's law with electric losses modeled by an electric conductivity and Faraday's law with a magnetic conductivity that models the magnetic losses can be time-stepped as a system of first order differential equations. Several electromagnetic field solvers in the time-domain exploit this form of Maxwell's equations. Taflove and Hagness [2] describe a conventional finite-difference time-domain (FDTD) scheme based on leap-frog time integration, which suffers from the staircase approximation inherent to the FDTD scheme formulated on structured (Cartesian) grids. Rodrigue and White [3] use hexahedral finite elements for the spatial discretization and time step the coupled Maxwell's equations with a leap-frog scheme, which gives a method that reduces to the FDTD scheme on rectilinear grids. The algorithm presented by Rodrigue and White [3] does not allow for unconditionally stable time-stepping and they do not consider tetrahedral meshes that are useful for local mesh refinement. Rieben, Rodrigue and White also published a similar method [4] that exploits higher order approximations for the spatial and temporal discretization. Riley and Jin [5] use finite-element (FE) techniques to discretize with respect to space and they arrive at a wave equation for the electric field that also involves the magnetic field. They use an explicit update algorithm of leap-frog type to compute the magnetic field by means of integration of Faraday's law. However, the time-stepping scheme used for the updating of the wave equation is not mentioned or described in their paper. Furthermore, their paper does not provide any information on the stability properties for their time-domain method.

A combination of the FDTD scheme applied to large homogeneous regions for efficiency and the finite-element method (FEM) for regions with complicated geometry and materials is attractive for many scattering problems. Wu and Itoh proposed FEM–FDTD hybridizations for both two [6] and three [7] dimensions. These schemes suffer from late-time instabilities that may be damped by temporal filtering [8]. Abenius et al. [9] combine the FDTD scheme with an implicit FEM and numerical studies indicate that it is stable, although no formal proof of stability is given. Monorchio et al. [10,11] proposed a hybrid that suffers from late-time instabilities and some attempts to mitigate this problem involve averaging or extrapolation techniques. Marrone and Mittra describe a way of interfacing triangles [12] and tetrahedrals [13] to FDTD cells but no explicit Courant criterion is derived. Rylander and Bondeson presented a stable FEM–FDTD hybrids [14,15] for 3D problems that are stable up to the Courant condition of the FDTD scheme, where convergence studies [15] and proofs of stability [15,16] are available in the literature. We emphasize that the treatment of magnetically lossy materials is not considered in any of these articles on hybrid FEM–FDTD algorithms.

There is a broad selection of numerical techniques that are formulated in the frequency domain [17,18], such as the method of moments (MoM) that may be accelerated by the multi-level fast multipole method (MLFMM) for electrically large scattering problems. The MoM is particularly efficient for scattering problems with many different incident angles. However, it provides the response for only one single frequency in contrast to time-domain field solvers that yield the response in a broad frequency-interval. The MoM can handle inhomogeneous materials and it may be formulated in the time domain, but such methods are computationally expensive and difficult to program. For problems that feature non-linear media, frequency domain methods in general and the MoM in particular are inappropriate, if not impossible, to use.

In this paper, we present a stable FEM–FDTD hybrid method for electromagnetic problems in two dimensions that feature complex geometry with materials that have both electric and magnetic losses. In contrast to what is available in the open literature on the FEM treatment of magnetic losses in combination with electric losses, our method is distinguished by a number of unique features: (i) an unconditionally stable time-stepping scheme based on FE techniques and Galerkin's method applied to the first order system of Ampère's and Faraday's law; (ii) a proof of stability for this type of implicit FEM; and (iii) a generalization of the stable FEM–FDTD hybrid [14] for 2D problems that is stable up to the Courant condition of the FDTD scheme. The unconditionally stable time-stepping scheme that we present in this paper, reduces to a special case of the conventional Newmark scheme [19] when it is applied to problems without magnetic losses. The FE techniques used to construct the unconditionally stable time-integration scheme offers the possibility to also treat dispersive materials [20]. In addition, we demonstrate that it is feasible to use the FEM–FDTD interface in regions that have both electric and magnetic losses. We would like to stress that the two-dimensional case is important for the design of wing profiles intended for stealth aircraft, and we will consider the corresponding 3D formulation in a future publication since the 3D Maxwell problem is significantly different from the 2D problem. For

the hybrid applied to the transverse electric (TE) case, the electric field is expanded in terms of linear edge elements and the magnetic field by piecewise constants – a construction that is feasible in 2D but yields an incorrect formulation for 3D problems since the 3D problem requires that the magnetic flux density is expanded in terms of divergence conforming elements [3,4,21]. The hybrid applied to the transverse magnetic (TM) case follows by duality.

We find it advantageous to treat the electric and magnetic losses by the implicitly time-stepped FEM for a number of reasons: (i) local mesh refinement can be used in the unstructured FEM region to resolve rapid variations in the electromagnetic field and/or the radar absorber's material parameters; (ii) the FDTD scheme is highly efficient for the free-space region; (iii) conventional FDTD techniques [2] such as the perfectly matched layer, Huygen's surface and near-to-far-field transformations can be directly applied in the FDTD region; (iv) it is possible to prove stability for this type of hybrid scheme; (v) the global time step is related to the highest frequency of interest and the Courant condition specifies an appropriate cell size for the free-space FDTD region; and (vi) the choice of the global time step does not depend on the cell size in the unstructured mesh. To summarize, our hybrid method combines the efficiency of the FDTD scheme with the excellent capabilities of the FEM to model curved boundaries, lossy inhomogeneous materials, rapid field variations and other challenges that are difficult to handle on structured grids with explicit time-stepping schemes. To the best of our knowledge, the hybrid algorithm for Maxwell equations with electric and magnetic losses that we propose has not been published in the open literature and it provides a unique combination of characteristic features that can not be offered by other existing methods.

2. The hybrid method

The two-dimensional cylinder scatterer typically consists of metal structures that are partially or completely covered by RAM for the purpose of reducing the RCS. This allows for an outer boundary designed with respect to e.g. aerodynamical performance. The metal is modeled as a perfect electric conductor (PEC) and the losses of the RAM by an electric conductivity σ_E and a corresponding magnetic conductivity σ_M. The conductivities σ_E and σ_M can be functions of the space coordinate and, analogously the permittivity $\varepsilon = \varepsilon_0 \varepsilon_r$ and the permeability $\mu = \mu_0 \mu_r$ can vary with respect to position in the RAM. The electromagnetic field for this situation satisfies Maxwell's equations

$$\nabla \times \boldsymbol{H} = \sigma_E \boldsymbol{E} + \varepsilon \frac{\partial \boldsymbol{E}}{\partial t} \tag{1a}$$

$$\nabla \times \boldsymbol{E} = -\mu \frac{\partial \boldsymbol{H}}{\partial t} - \sigma_M \boldsymbol{H}. \tag{1b}$$

The FEM–FDTD algorithm for this problem is presented for the TE case and the TM case follows from duality. It should be emphasized that the FEM–FDTD hybrid allows for *both* magnetic and electric losses at the interface between the FEM region and the FDTD region.

2.1. Spatial discretization

The domain Ω is subdivided by a structured Cartesian grid of rectangles in large homogeneous regions and an unstructured mesh of triangles in the vicinity of curved boundaries, where the boundary of Ω is denoted Γ. At the interface that connects the structured and unstructured discretizations each edge is shared by one rectangle and one triangle. We expand the electric field in terms of linear edge elements [17,21] and they are denoted by $\boldsymbol{w}_j$ in the following. The magnetic field is expanded in piecewise constants denoted $\boldsymbol{f}_j$. (In what follows, it is rather straight forward to replace $\boldsymbol{w}_j$ and $\boldsymbol{f}_j$ by the corresponding higher-order curl- and divergence-conforming elements, should a higher-order method with respect to space be more desirable. A hierarchical basis [22] could be used if linear elements close to singularities are to be combined with higher order elements elsewhere.) We use Galerkin's method to derive the weak form

$$\langle \boldsymbol{w}_i, \hat{n} \times \boldsymbol{H} \rangle_\Gamma + (\nabla \times \boldsymbol{w}_i, \boldsymbol{H})_\Omega = (\boldsymbol{w}_i, \sigma_E \boldsymbol{E})_\Omega + \frac{\partial}{\partial t} (\boldsymbol{w}_i, \varepsilon \boldsymbol{E})_\Omega \tag{2a}$$

$$(\boldsymbol{f}_i, \nabla \times \boldsymbol{E})_\Omega = -\frac{\partial}{\partial t}(\boldsymbol{f}_i, \mu\boldsymbol{H})_\Omega - (\boldsymbol{f}_i, \sigma_M\boldsymbol{H})_\Omega \qquad (2b)$$

where $(\boldsymbol{u}, \boldsymbol{v})_\Omega = \int_\Omega \boldsymbol{u} \cdot \boldsymbol{v} \, d\Omega$ and $\langle \boldsymbol{u}, \boldsymbol{v} \rangle_\Gamma = \oint_\Gamma \boldsymbol{u} \cdot \boldsymbol{v} \, d\Gamma$.

2.2. Time-stepping scheme

The temporal discretization is also based on FE techniques. This makes it feasible to generalize the proposed method to problems that involve dispersive materials by means of the techniques described in Ref. [20]. In the following, we denote the time-dependent coefficients $e_j(t)$ for the electric field and $h_j(t)$ for the magnetic field.

In the FE region with triangles, we choose $e_j(t)$ and $h_j(t)$ to be piecewise linear in time and let the temporal degrees of freedom be associated with the grid points $t^{(n)} = n\Delta t$ of the integer mesh $n = 0, 1, 2, \ldots$, where n is the time index and Δt is the time step. Thus, $e_j(t)$ and $h_j(t)$ are expanded in terms of the linear basis functions $l^{(n)}(t)$. Fig. 1 shows a selection of the temporal basis and test functions. An implicit time-stepping scheme is constructed for the FE region by means of piecewise constant $c^{(n+1/2)}(t)$ test functions with respect to time for (2a) and (2b). The test function $c^{(n+1/2)}(t)$ is unity on the time interval $n\Delta t < t < (n+1)\Delta t$ and zero otherwise, which yields a test function that is centered on the half mesh with respect to time. This procedure results in a time-stepping scheme that provides unconditionally stable time-stepping for problems with both electric and magnetic losses. For the special case without magnetic losses, it reduces to the conventional Newmark scheme [19] with the implicitness parameter $\theta = 1/4$.

For the remaining degrees of freedom, we choose $e_j(t)$ to be piecewise linear and centered on the integer mesh in combination with $h_j(t)$ expanded in piecewise constant basis functions centered on the half mesh. In the structured region, we use piecewise constant test functions $c^{(n+1/2)}(t)$ for Ampère's law (2a) and piecewise linear test functions $l^{(n)}(t)$ for Faraday's law (2b). The explicit leap-frog time-stepping method of the FDTD scheme is recovered by trapezoidal integration for Faraday's law (2b) and stable time-stepping is possible when the time step Δt fulfills the Courant condition of the FDTD scheme, see Refs. [2,23] for detailed discussions on the stability of the FDTD scheme.
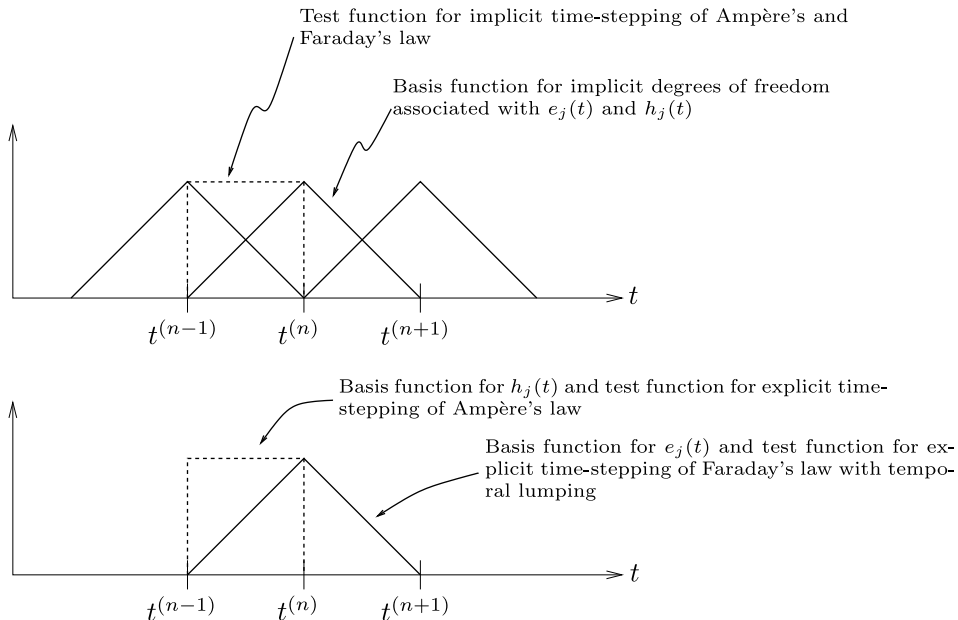

Fig. 1. Implicit unconditionally stable scheme: piecewise linear expansion of $e_j(t)$ and $h_j(t)$; and piecewise constant test functions for Ampère's and Faraday's law. Explicit leap-frog scheme: piecewise linear expansion of $e_j(t)$ and test function for Faraday's law with temporal lumping; and piecewise constant expansion of $h_j(t)$ and test function for Ampère's law.

For spatial test functions $\mathbf{w}_i$ and $\mathbf{f}_i$ associated with the unstructured mesh of triangles, the field representation substituted into Ampère's law (2a) and Faraday's law (2b) yields the time-stepping scheme

$$\begin{bmatrix} \mathbf{M}_\varepsilon + \frac{\Delta t}{2} \mathbf{B}_E & -\frac{\Delta t}{2} \mathbf{C}^T \\ \frac{\Delta t}{2} \mathbf{C} & \mathbf{M}_\mu + \frac{\Delta t}{2} \mathbf{B}_M \end{bmatrix} \mathbf{x}^{(n)} = \begin{bmatrix} \mathbf{M}_\varepsilon - \frac{\Delta t}{2} \mathbf{B}_E & \frac{\Delta t}{2} \mathbf{C}^T \\ -\frac{\Delta t}{2} \mathbf{C} & \mathbf{M}_\mu - \frac{\Delta t}{2} \mathbf{B}_M \end{bmatrix} \mathbf{x}^{(n-1)} \tag{3}$$

where

$$(\mathbf{C})_{ij} = (\mathbf{f}_i, \nabla \times \mathbf{w}_j)_\Omega \ (\mathbf{B}_E)_{ij} = (\mathbf{w}_i, \sigma_E \mathbf{w}_j)_\Omega \ (\mathbf{M}_\varepsilon)_{ij} = (\mathbf{w}_i, \varepsilon \mathbf{w}_j)_\Omega$$
$$(\mathbf{B}_M)_{ij} = (\mathbf{f}_i, \sigma_M \mathbf{f}_j)_\Omega \ (\mathbf{M}_\mu)_{ij} = (\mathbf{f}_i, \mu \mathbf{f}_j)_\Omega.$$

Here, $\mathbf{x}^{(n)}$ is a vector with (i) all the degrees of freedom $e_j^{(n)}$ and $h_j^{(n)}$ associated with the unstructured triangles; and (ii) the field represented by $h_j^{(n-1/2)}$ on the structured mesh of rectangles that feature when Ampère's law (1a) is tested by $\mathbf{w}_i$ associated with edges shared by triangles and rectangles on the interface between the implicit unstructured mesh and the explicit structured grid.

2.3. Stability for the FEM–FDTD interface

In this article, we demonstrate that our hybrid interface is stable when it is applied to material regions with both electric and magnetic losses. For regions with a sufficiently large conductivity, the problem is stiff [24] and it is advantageous to use the implicit time-stepping scheme associated with the FEM region rather than the explicit FDTD scheme. The interface exploited in a vacuum region is identical to the stable FEM–FDTD hybrid [14] for the implicitness parameter $\theta = 1/4$. In this case, Belytschko and Mullen [16] show that the discrete energy is bounded if the Courant condition of the explicit time-stepping scheme is fulfilled.

2.4. Analysis of the time-domain FEM with both electric and magnetic losses

The presence of magnetic losses makes the usage of conventional time-stepping schemes a challenge when the second-order wave equation is considered. An attempt to address this issue in the literature can be found in Ref. [5]. Here, we demonstrate some differences between our hybrid method and the scheme discussed in Ref. [5]. Consider a problem with electric and magnetic losses, where the time-stepping scheme (3) is applied to the entire computational domain. Let $\mathbf{x}$ denote an eigenmode with the growth factor ρ such that $\mathbf{x}^{(n)} = \rho^n \mathbf{x}$, which allows for von Neumann analysis at the frequency ω when $\rho = \exp(j\omega\Delta t)$. The time-stepping scheme (3) with $\mathbf{x}^{(n)} = \rho^n \mathbf{x}$ yields

$$\rho \begin{bmatrix} \mathbf{M}_\varepsilon + \frac{\Delta t}{2} \mathbf{B}_E & -\frac{\Delta t}{2} \mathbf{C}^T \\ \frac{\Delta t}{2} \mathbf{C} & \mathbf{M}_\mu + \frac{\Delta t}{2} \mathbf{B}_M \end{bmatrix} \mathbf{x} = \begin{bmatrix} \mathbf{M}_\varepsilon - \frac{\Delta t}{2} \mathbf{B}_E & \frac{\Delta t}{2} \mathbf{C}^T \\ -\frac{\Delta t}{2} \mathbf{C} & \mathbf{M}_\mu - \frac{\Delta t}{2} \mathbf{B}_M \end{bmatrix} \mathbf{x}, \tag{4}$$

where the vector $\mathbf{x}$ contains the electromagnetic field (i.e. the electric field $\mathbf{e}$ and the magnetic field $\mathbf{h}$) such that its complex conjugate transpose is $\mathbf{x}^H = [\mathbf{e}^H, \mathbf{h}^H]$. We eliminate the magnetic field from the system (4) of Ampère's and Faraday's law, which yields the Helmholtz equation for the electric field

$$\mathbf{C}^T \left[\mathbf{M}_\mu + \frac{\rho + 1}{\rho - 1} \frac{\Delta t}{2} \mathbf{B}_M \right]^{-1} \mathbf{C} \left(\frac{\rho^2 + 2\rho + 1}{4} \mathbf{e} \right) = -\mathbf{M}_\varepsilon \left(\frac{\rho^2 - 2\rho + 1}{(\Delta t)^2} \mathbf{e} \right) - \mathbf{B}_E \left(\frac{\rho^2 - 1}{2\Delta t} \mathbf{e} \right). \tag{5}$$

The term on the left-hand side in Eq. (5) corresponds to $\nabla \times [(\mu + \sigma_M/(j\omega))^{-1} \nabla \times \mathbf{E}(\mathbf{r}, \omega)]$, which can be illustrated by $\rho = \exp(j\omega\Delta t)$ with $\omega\Delta t \ll 1$ that yields

$$\frac{\rho + 1}{\rho - 1} \frac{\Delta t}{2} = \frac{(1 + j\omega\Delta t + \cdots) + 1}{(1 + j\omega\Delta t + \cdots) - 1} \frac{\Delta t}{2} \simeq \frac{1}{j\omega}.$$

For the left-hand side of Eq. (5), the product of the electric field and a frequency dependent material parameter (that may also depend on the space coordinate) implies that the corresponding time-domain wave equation includes a convolution. This aspect should be addressed if the second-order wave equation is targeted – an approach that is attempted in Ref. [5]. We emphasize that the time-integration scheme (3) that we propose

does not feature any convolutions, which we regard as a distinct advantage. Moreover, we avoid having to deal with the curl of discontinuous functions that features in Ref. [5].

Finally, we rewrite Eq. (4) so that it reads

$$\frac{\rho - 1}{\Delta t} \begin{bmatrix} \mathbf{M}_\varepsilon & 0 \\ 0 & \mathbf{M}_\mu \end{bmatrix} \begin{bmatrix} \mathbf{e} \\ \mathbf{h} \end{bmatrix} + \frac{\rho + 1}{2} \begin{bmatrix} \mathbf{B}_E & 0 \\ 0 & \mathbf{B}_M \end{bmatrix} \begin{bmatrix} \mathbf{e} \\ \mathbf{h} \end{bmatrix} = \frac{\rho + 1}{2} \begin{bmatrix} 0 & \mathbf{C}^T \\ -\mathbf{C} & 0 \end{bmatrix} \begin{bmatrix} \mathbf{e} \\ \mathbf{h} \end{bmatrix}. \tag{6}$$

Eq. (6) is multiplied from the left by $\mathbf{x}^H = [\mathbf{e}^H, \mathbf{h}^H]$ and we get

$$\frac{2\zeta}{\Delta t} \left(\mathbf{e}^H \mathbf{M}_\varepsilon \mathbf{e} + \mathbf{h}^H \mathbf{M}_\mu \mathbf{h} \right) + \mathbf{e}^H \mathbf{B}_E \mathbf{e} + \mathbf{h}^H \mathbf{B}_M \mathbf{h} = \mathbf{e}^H \mathbf{C}^T \mathbf{h} - \mathbf{h}^H \mathbf{C} \mathbf{e}, \tag{7}$$

where $\zeta = (\rho - 1)/(\rho + 1)$. Stability requires that $|\rho| \leqslant 1$ for all modes, which is equivalent to $\mathrm{Re}\{\zeta\} \leqslant 0$ for all modes. (Here, negative values for $\mathrm{Re}\{\zeta\}$ correspond to damped modes with $|\rho| < 1$.) We note that the right-hand side of Eq. (7) is purely imaginary, since $\mathbf{e}^H \mathbf{C}^T \mathbf{h} - \mathbf{h}^H \mathbf{C} \mathbf{e} = -2\mathrm{j}\,\mathrm{Im}\{\mathbf{h}^H \mathbf{C} \mathbf{e}\}$. The matrices $\mathbf{M}_\varepsilon$ and $\mathbf{M}_\mu$ are real, symmetric and positive definite. Furthermore, $\mathbf{B}_E$ and $\mathbf{B}_M$ are real, symmetric and semi-positive definite. Thus, the real part of Eq. (7) yields

$$\mathrm{Re}\{\zeta\} = -\frac{\Delta t}{2} \frac{\mathbf{e}^H \mathbf{B}_E \mathbf{e} + \mathbf{h}^H \mathbf{B}_M \mathbf{h}}{\mathbf{e}^H \mathbf{M}_\varepsilon \mathbf{e} + \mathbf{h}^H \mathbf{M}_\mu \mathbf{h}} \leqslant 0. \tag{8}$$

Consequently, the lossless case $\mathbf{e}^H \mathbf{B}_E \mathbf{e} + \mathbf{h}^H \mathbf{B}_M \mathbf{h} = 0$ yields $\mathrm{Re}\{\zeta\} = 0$ which corresponds to undamped modes with $|\rho| = 1$. For problems with electric and/or magnetic losses, we have $\mathbf{e}^H \mathbf{B}_E \mathbf{e} + \mathbf{h}^H \mathbf{B}_M \mathbf{h} \geqslant 0$, i.e. $\mathrm{Re}\{\zeta\} < 0$ for modes that are non-zero in the lossy region and such modes are damped since $|\rho| < 1$. This shows that the time-stepping scheme (3) provides stable time-stepping for the case with both electric and magnetic losses. To conclude, the time-stepping scheme (3) can be used for a standard time-domain FEM with unconditionally stable time-stepping. In addition, it can be exploited in a hybrid setting (for more efficient computations) together with the FDTD scheme as described in this article.

3. Numerical results

In order to verify the accuracy and convergence properties of the hybrid method, we apply the method to three different test problems. The first problem consists of a circular metal cylinder with a lossy coating. The second problem is a homogeneous lossy circular cylinder. The RCS can be calculated analytically for both these problems. The third problem is a metal airfoil with its leading edge covered by a lossy material. In all problems, the scatterer is illuminated by a plane wave that is inserted at a Huygen's surface [2]. The amplitude of the incident wave is given by

$$E_{\mathrm{inc}}(t) = E_0 \exp\left(-\frac{(t - \tau)^2}{T^2}\right) \sin(\omega_c (t - \tau)), \tag{9}$$

i.e. a sinusoidal with the center frequency $\omega_c = 2\pi f_c$ that is amplitude modulated with a Gaussian. For the frequency ω, the Fourier transform of the time-domain fields gives the RCS in two dimensions as [25]

$$\sigma = \lim_{r \to \infty} 2\pi r \frac{|\boldsymbol{E}_{\mathrm{sc}}(\omega)|^2}{|\boldsymbol{E}_{\mathrm{inc}}(\omega)|^2} \tag{10}$$

where $\boldsymbol{E}_{\mathrm{sc}}$ is the scattered electric field and $\boldsymbol{E}_{\mathrm{inc}}$ is the incident plane wave. The incident plane wave propagates in the direction $\hat{k}_{\mathrm{inc}} = \hat{x} \cos \varphi_{\mathrm{inc}} + \hat{y} \sin \varphi_{\mathrm{inc}}$, where the angle of incidence φ_{inc} is measured counter clockwise from the positive x-axis. A near-to-far field transformation [2] is used to compute the scattered field $\boldsymbol{E}_{\mathrm{sc}}$ for observation points $\boldsymbol{r} = \hat{r}(\varphi_{\mathrm{sc}})r = \hat{x}r \cos \varphi_{\mathrm{sc}} + \hat{y}r \sin \varphi_{\mathrm{sc}}$ far from the scatterer. In the far-field region, the electric field is $\boldsymbol{E}_{\mathrm{sc}}(r, \varphi_{\mathrm{sc}}) = r^{-1/2} \exp(-\mathrm{j}k_0 r) \boldsymbol{F}(\varphi_{\mathrm{sc}})$, where

$$\boldsymbol{F}(\varphi_{\mathrm{sc}}) = \frac{\omega \mu_0 \, \mathrm{e}^{\mathrm{j}\pi/4}}{\sqrt{8\pi k_0}} \oint_{C_a} \left(\hat{r} \times \hat{r} \times [\hat{n} \times \boldsymbol{H}(\boldsymbol{r}')] - \frac{1}{\eta_0} \hat{r} \times [\hat{n} \times \boldsymbol{E}(\boldsymbol{r}')] \right) \mathrm{e}^{\mathrm{j}k_0 \hat{r} \cdot \boldsymbol{r}'} \, \mathrm{d}C'$$

is a scattering amplitude and C_a is the near-to-far field transformation surface. Here, the intrinsic impedance of free space is $\eta_0 = \sqrt{\mu_0/\varepsilon_0}$ and the corresponding wave number is $k_0 = \omega\sqrt{\mu_0\varepsilon_0}$. We denote the unit normal to the closed contour C_a by $\hat{n}$.

Outside the near-to-far field transformation surface, the scattered field is absorbed by a perfectly matched layer [2] (PML) enclosed in a PEC box. In the first and the second test problem, the PML is 16 cells thick and in the third test problem the thickness is 12 cells, all specified on the coarsest grid. The physical thickness of the PML is constant as the grids are refined. The conductivity profile of the PML is given by $\sigma = \sigma_{\max}(\xi/\delta)^{3.5}$, where ξ is the perpendicular distance to the PML–air-interface and δ is the thickness of the PML. We use $\sigma_{\max} = 2.55 \times 10^{-2}$ S/m for the first and the second test problem and $\sigma_{\max} = 5.42 \times 10^{-1}$ S/m for the third problem.

3.1. Test 1 – bistatic RCS for a coated PEC cylinder

First, consider scattering from a circular PEC cylinder with a lossy coating. The FEM–FDTD hybrid is exploited to compute the time-domain response and the RCS is evaluated at the frequency $f_c = 100$ MHz. The radius of the PEC cylinder is $a = 0.9\lambda_c$, where λ_c is the free-space wavelength at the center frequency. The thickness of the lossy coating is $b - a = 0.1\lambda_c$, where b is the radius for the circular boundary between the coating and the free space. The lossy coating is characterized by the material parameters $\varepsilon_r = \mu_r = 3$ and $\sigma_E/\varepsilon_0 = \sigma_M/\mu_0 = 2\omega_c$. This problem has an analytical solution and its RCS is given by

$$\sigma_{TE} = \frac{4}{k_0}\left|\sum_{n=-\infty}^{\infty} \frac{J_n'(k_0 b) + G_n^{TE} J_n(k_0 b)}{H_n^{(2)'}(k_0 b) + G_n^{TE} H_n^{(2)}(k_0 b)} e^{jn\varphi_{sc}}\right|^2$$

$$\sigma_{TM} = \frac{4}{k_0}\left|\sum_{n=-\infty}^{\infty} \frac{J_n'(k_0 b) + G_n^{TM} J_n(k_0 b)}{H_n^{(2)'}(k_0 b) + G_n^{TM} H_n^{(2)}(k_0 b)} e^{jn\varphi_{sc}}\right|^2$$

where

$$G_n^{TE} = -\sqrt{\frac{\mu_r}{\varepsilon_r}}\frac{J_n'(k_1 b)Y_n'(k_1 a) - J_n'(k_1 a)Y_n'(k_1 b)}{J_n(k_1 b)Y_n'(k_1 a) - J_n'(k_1 a)Y_n(k_1 b)}$$

$$G_n^{TM} = -\sqrt{\frac{\varepsilon_r}{\mu_r}}\frac{J_n(k_1 a)Y_n'(k_1 b) - J_n'(k_1 b)Y_n(k_1 a)}{J_n(k_1 a)Y_n(k_1 b) - J_n(k_1 b)Y_n(k_1 a)}$$

and k_1 is the wave number in the lossy coating. Wang [26] published analytical results for the case when $\mu_r = 1$.

The FEM–FDTD hybrid is used to compute the bistatic RCS of the circular cylinder when it is illuminated by a plane wave temporally described by the amplitude (9) with $T = \sqrt{2}/(30\pi \times 10^6)$ s and $\tau = 4T$. Fig. 2 shows the relative error $\|\sigma - \sigma^*\|/\|\sigma^*\|$ as a function of resolution for the TE polarization by the solid curve and TM polarization by the dashed curve, where σ is the computed RCS and σ^* is the analytical RCS. Here, we use the norm $\|\cdot\| = [\int_0^{2\pi}(\cdot)^2 \, d\varphi_{sc}]^{1/2}$. The computation was performed for the resolutions $\lambda_c/h = 8, 16, 32, 64$ and 96, where the time step is $\Delta t = h/(\sqrt{2}c_0)$, and the FDTD cell size is denoted h. (The triangular mesh has a typical cell size that is somewhat smaller than h and we use a hierarchical refinement as the resolution is increased.) The solution to this field problem is regular and we achieve second-order convergence with respect to the cell size as expected for a numerical scheme based on a linear field approximation. An accuracy of 2% is achieved for about 20 points per wavelength.

3.2. Test 2 – bistatic RCS for a homogeneous lossy cylinder

The second test case consists of a homogeneous lossy circular cylinder. The radius of the cylinder is λ_c and the material parameters are $\varepsilon_r = \mu_r = 2$ and $\sigma_E/\varepsilon_0 = \sigma_M/\mu_0 = 0.1\omega_c$. As for the first test case, this scattering problem can be solved analytically and, again, we perform a convergence study.

Here, we discretize a thin layer in the vicinity of the circular boundary by the FEM. Thus, the main part of the cylinder's interior with the homogeneous lossy material is discretized by the FDTD scheme and can be
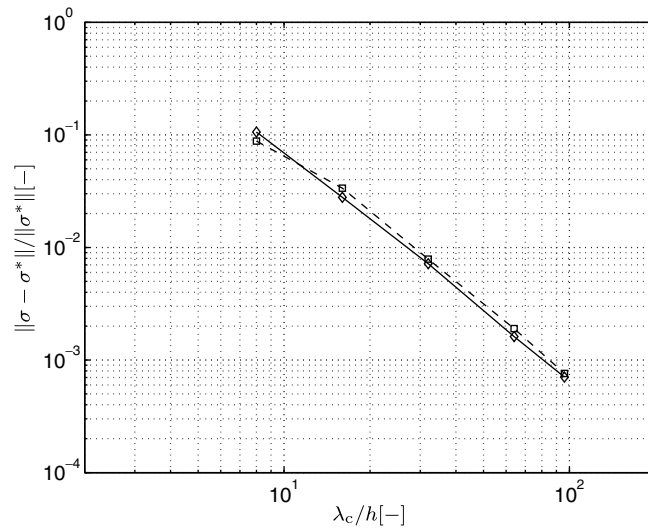
Fig. 2. The relative error in the bistatic RCS as a function of resolution for a circular cylinder with a lossy coating: TE polarization – solid curve and TM polarization – dashed curve.

updated explicitly. Consequently, this test problem has two hybrid FEM–FDTD interfaces: (i) the interface in the vacuum region; and (ii) the interface *inside* the lossy cylinder.

Fig. 3 shows the relative error $\|\sigma - \sigma^*\|/\|\sigma^*\|$ as a function of resolution for the TE polarization, where the general setup for the FEM–FDTD computation is the same as in the first test case. The computation was performed for the resolutions $\lambda_c/h = 16, 32$ and 64. We emphasize that the hybrid computation is stable and that we achieve second-order convergence with respect to the cell size towards the analytical solution.

3.3. Test 3 – monostatic RCS for an airfoil

The third test case deals with scattering from the airfoil depicted in Fig. 4, where the illuminating plane wave is temporally described by the amplitude (9) with $f_c = 850$ MHz, $T = \sqrt{2}/(250\pi \times 10^6)$ s and $\tau = 4T$. The airfoil consists of a PEC core with a RAM placed on its leading edge. The absorbing material is charac-
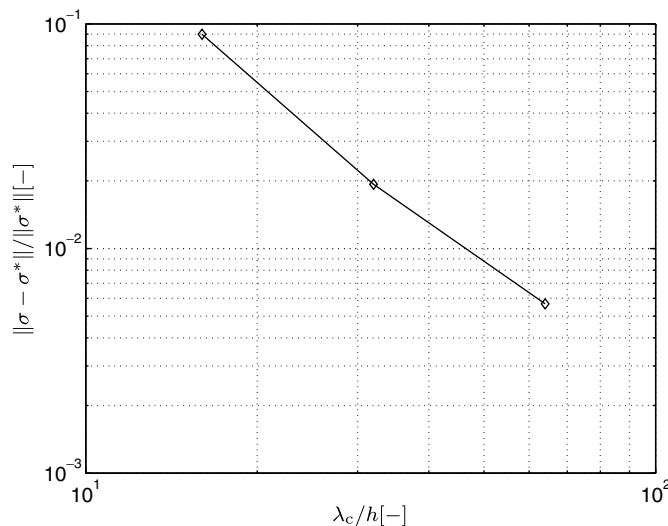

Fig. 3. The relative error in the bistatic RCS as a function of resolution for a homogeneous lossy circular cylinder; TE polarization.
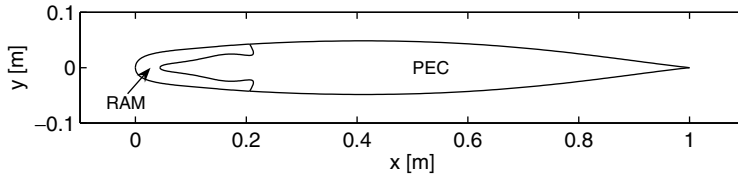
Fig. 4. The geometry of the airfoil that consists of a PEC structure with a RAM placed on its leading edge.

terized by the parameters $\varepsilon_r = 2.13$, $\mu_r = 4.14$, $\sigma_E/\varepsilon_0 = 2.14\omega_c$ and $\sigma_M/\mu_0 = 0.73\omega_c$. These material parameters and the shape of the PEC-RAM boundary are optimized [27] to achieve a low RCS for $-20° < \varphi_{inc} < 20°$ and 600 MHz $< f <$ 1100 MHz. The geometry of the wing is described by Bézier curves [28]. The wing is symmetric with respect to $y = 0$ and the three Bézier curves that are used to describe the shape in the region $y < 0$ have the control points $\mathbf{c}_i$ shown in Table 1.

Fig. 5 shows the monostatic RCS for the TM polarization as a function of the incident angle φ_{inc} for three different frequencies: 600 MHz-solid curve; 850 MHz-dashed curve and 1100 MHz – dash-dotted curve. The corresponding results for the TE case are shown in Fig. 6. The monostatic RCS requires that $\varphi_{sc} = \varphi_{inc} + \pi$ and in the following we use $\varphi = \varphi_{inc}$. Here, the scattering amplitude $\mathbf{F}$ is computed on a grid with $h = \lambda_c/60$ for a set of $M + 1$ incident angles $\varphi_i = i\Delta\varphi$, where $i = 0, 1, \ldots, M$ and $\Delta\varphi = \pi/M$. The computed $\mathbf{F}(\varphi_i)$ is then interpolated by a Fourier series.

Table 1
Control points for the Bézier curves that are used for the geometrical description of the airfoil

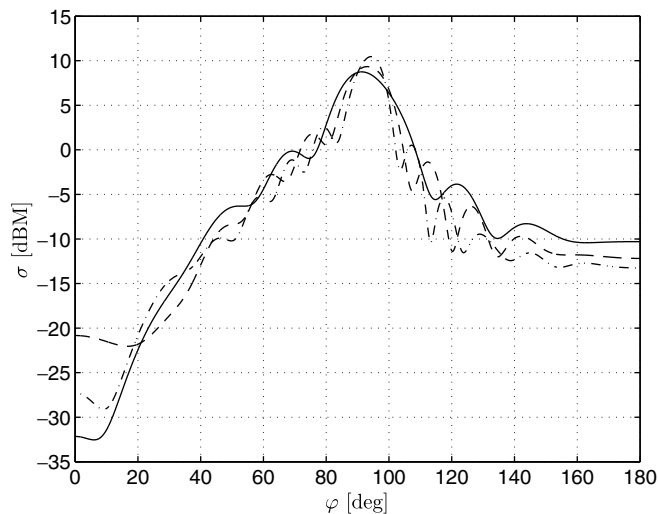| Curve 1	Curve 2	Curve 3
$(1.0000, 0)$	$(0.20617, -0.042504)$	$(0.20617, -0.042504)$
$(0.82896, -0.018792)$	$(0.12904, -0.038207)$	$(0.23675, 0.0083209)$
$(0.60266 0.064594)$	$(0.071682, -0.028602)$	$(0.17220, -0.048014)$
$(0.20617, -0.042504)$	$(0, -0.034171)$	$(0.13631, -0.029701)$
	$(0, 0)$	$(0.15374, -0.0026923)$
		$(0.044322, -0.015023)$
		$(0.044322, 0)$

Fig. 5. Monostatic RCS σ for the TM polarization as a function of the incident angle φ: 600 MHz – solid curve; 850 MHz – dashed curve and 1100 MHz – dash-dotted curve.
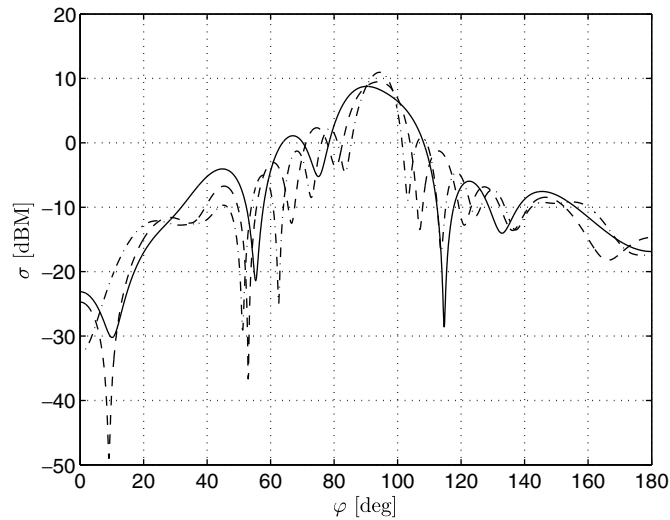
Fig. 6. Monostatic RCS σ for the TE polarization as a function of the incident angle φ: 600 MHz – solid curve; 850 MHz – dashed curve and 1100 MHz – dash-dotted curve.

The airfoil features sharp material corners and we expect a singular field solution at these points. In order to investigate the convergence properties of the FEM–FDTD hybrid algorithm, we performed computations with a number of different FDTD grids with $h = h_0/n_h$, where $h_0 = \lambda_c/20$ and $n_h = 1, 2, \ldots, 7$. Analogously, the FEM mesh of triangles is refined in a hierarchical manner. The trailing edge of the wing is a PEC corner in a homogeneous region, where $\varepsilon = \varepsilon_0$ and $\mu = \mu_0$. The PEC corner subtends an angle $\beta = 0.2189$ and an analytical treatment [29] yields that the scattering amplitude converge, to the lowest order, as $\boldsymbol{F}(h) = \boldsymbol{F}_0 + \boldsymbol{F}_\alpha h^\alpha$, where $\alpha = (1 - \beta/(2\pi))^{-1} = 1.036$ is the order of convergence. Here, $\boldsymbol{F}_0$ denotes the extrapolated result and, for a given α, it can be estimated (together with the coefficients $\boldsymbol{F}_\alpha$) by a least square fit to the amplitudes $\boldsymbol{F}_h$ computed by the FEM–FDTD hybrid with cell size h. Fig. 7 shows the error $e(\alpha) = \sum_h \|\boldsymbol{F}(h) - \boldsymbol{F}_h\|^2$ as a function of α for different sets of resolution in the case of the TM polarization. The lowest error is achieved for
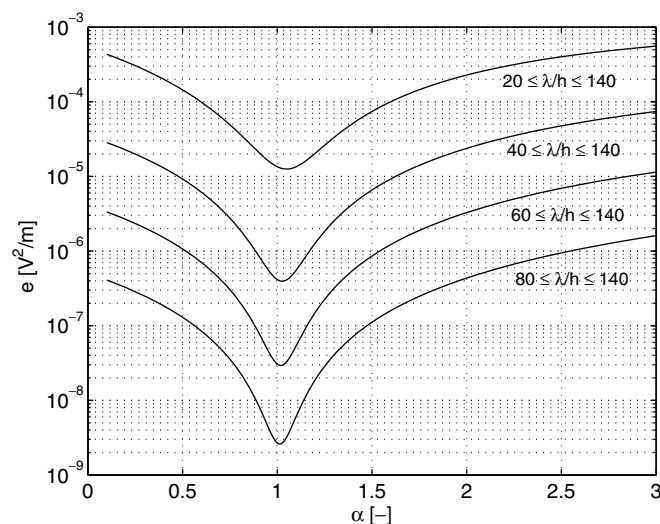

Fig. 7. Fit of the error $e(\alpha) = \sum_h \|\boldsymbol{F}(h) - \boldsymbol{F}_h\|^2$ as a function of the exponent α in the extrapolation model $\boldsymbol{F}(h) = \boldsymbol{F}_0 + \boldsymbol{F}_\alpha h^\alpha$, where $\boldsymbol{F}_0$ and $\boldsymbol{F}_\alpha$ are computed by a least square fit. Here, $\boldsymbol{F}_h$ denotes the result computed by the FEM–FDTD hybrid for the cell size h and the error is shown for different resolutions λ/h included in the error sum.
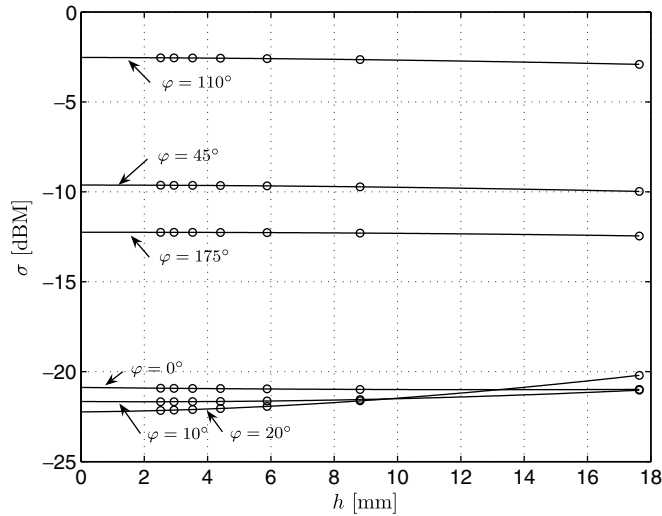
Fig. 8. Convergence of the monostatic RCS σ for TM polarization with respect to the cell size h for different angles of incidence φ: computed results – circles; fit for extrapolation – solid curves.

$\alpha = 1.01$ when $80 \leqslant \lambda/h \leqslant 140$. This order of convergence is within 3% from the expected $\alpha = 1.036$. A fit that also includes scattering amplitudes computed at lower resolutions yields a larger error and larger values for its minimum with respect to α, which is expected since the dispersion error that scales as h^2 (and higher-order terms) becomes more dominant on coarser grids. A similar study based on the extrapolation model $\boldsymbol{F}(h) = \boldsymbol{F}_0 + \boldsymbol{F}_\alpha h^\alpha + \boldsymbol{F}_\beta h^\beta$ with $\alpha = 1.01$ fixed gives rather flat error curves with respect to β, where a shallow minimum can be found around $\beta = 2.09$ for $20 \leqslant \lambda/h \leqslant 140$ and $\beta = 2.02$ for $80 \leqslant \lambda/h \leqslant 140$. We conclude that the model $\boldsymbol{F}(h) = \boldsymbol{F}_0 + \boldsymbol{F}_\alpha h^\alpha$ with $\alpha = 1.01$ fixed gives a good fit and extend this with a term $\boldsymbol{F}_2 h^2$ that captures the dispersion errors. In principle, the two points where the RAM, the PEC and the air region join also support singularities [30] but the amplitudes for such error terms appear to be small in this context given the computed results. The same conclusion is reached for the TE case.

Fig. 8 shows the RCS for the TM case with respect to h for the angles $\varphi = 0°, 10°, 20°, 45°, 110°$ and $175°$, where the computed results are shown by circles and the fitted extrapolation models are shown by solid curves. It is noticed that for some angles such as $\varphi = 20°$, the RCS is relatively sensitive to the discretization errors and it varies substantially as the resolution is increased.

Given the extrapolated results σ_0, we study the deviation $\Delta\sigma = 10\log_{10}(\sigma/\sigma_0)$ for the computed results σ as a function of φ. For the frequency 850 MHz, the deviation is less than 1 dB for at least 90% of the azimuths at the coarsest grid and the large deviations coincide with deep minima in the RCS. We tentatively estimate the error in our extrapolated results to be less than 0.1 dB, except for azimuth angles that correspond to very deep minima in the RCS.

4. Conclusions

We have presented a stable FEM–FDTD hybrid in two dimensions that allows for both electric and magnetic losses. For the transverse electric (TE) case, the electric field is expanded in linear edge elements on the computational domain, and the magnetic field is expressed in terms of piecewise constant basis functions. The transverse magnetic (TM) case follows from duality. The computational domain is divided in two parts: (i) homogeneous space discretized by a structured grid of rectangles; and (ii) the remaining regions in the vicinity of curved boundaries discretized by an unstructured mesh of triangles. For the FEM region, an unconditionally stable implicit time-stepping scheme is used. The global time-step is limited by the Courant condition for the explicit FDTD scheme on the structured grid. The FEM–FDTD interface is constructed as to ensure stability.

The scheme is tested on three scattering problems. In the first problem, we compute the bistatic radar cross section (RCS) for a circular metal cylinder with a lossy coating. For both the TE and TM polarization, the bistatic RCS shows second-order convergence to the analytical solution with respect to cell size, and a resolution of about 20 points per wavelength yields a relative error below 2%. The second problem consists of a homogeneous lossy circular cylinder, where an annular layer in the vicinity of the circular boundary is treated by the FEM and the homogeneous regions exterior and interior to the annular FEM region are treated by the FDTD scheme. The bistatic RCS is computed for the TE polarization and it shows second-order convergence to the analytical solution with respect to cell size. The third problem deals with scattering from an airfoil with an absorbing material on its leading edge. Bézier curves are used to describe the geometry of the scatterer. The Fourier spectrum of the monostatic RCS with respect to the incident angle demonstrates that the scattered field can be represented by a limited number of Fourier modes. Hence, a suitable interpolation model with respect to the azimuth angle is constructed by means of a Fourier series. An extrapolation model for the numerical error yields an order of convergence that agrees well with what is expected given the field singularities at sharp corners and dispersion errors. The deviation in the computed RCS from the extrapolated results is less than 1 dB for at least 90 % of the incident angles for a resolution as low as 20 points per wavelength. The detailed geometry description and accurate results presented in this article makes this test case an appropriate reference problem for 2D RCS codes that model both electric and magnetic losses. We conclude that the stable FEM–FDTD hybrid is robust and yields accurate results.

References

[1] H. Mosallaei, Y. Rahmat-Samii, RCS reduction of canonical targets using genetic algorithm synthesized RAM, IEEE Trans. Antennas Propag. 48 (10) (2000) 1594–1606.

[2] A. Taflove, S.C. Hagness, Computational Electrodynamics: The Finite-Difference Time-Domain Method, second ed., Artech House, Northwood, MA, 2000.

[3] G. Rodrigue, D. White, A vector finite element time-domain method for solving Maxwell's equations on unstructured hexahedral grids, SIAM J. Sci. Comput. 23 (3) (2001) 683–706.

[4] R.N. Rieben, G.H. Rodrigue, D.A. White, A high order mixed vector finite element method for solving the time dependent Maxwell equations on unstructured grids, J. Comput. Phys. 204 (2) (2005) 490–519, doi:10.1016/j.jcp.2004.10.030.

[5] D.J. Riley, J.-M. Jin, Modeling of magnetic loss in the finite-element time-domain method, Microw. Opt. Technol. Lett. 46 (2) (2005) 165–168, doi:10.1002/mop.20932.

[6] R.-B. Wu, T. Itoh, Hybridizing FD-TD analysis with unconditionally stable FEM for objects of curved boundary, IEEE MTT-S Int. Microw. Symp. Digest 2 (1995) 833–836, doi:10.1109/MWSYM.1995.405918.

[7] R.-B. Wu, T. Itoh, Hybrid finite-difference time-domain modeling of curved surfaces using tetrahedral edge elements, IEEE Trans. Antennas Propag. 45 (8) (1997) 1302–1309, doi:10.1109/8.611251.

[8] C.-T. Hwang, R.-B. Wu, Treating late-time instability of hybrid finite-element/finite-difference time-domain method, IEEE Trans. Antennas Propag. 47 (2) (1999) 227–232, doi:10.1109/8.761061.

[9] E. Abenius, U. Andersson, F. Edelvik, L. Eriksson, G. Ledfelt, Hybrid time domain solvers for the Maxwell equations in 2D, Int. J. Numer. Methods Eng. 53 (9) (2002) 2185–2199, doi:10.1002/nme.380.

[10] A. Monorchio, R. Mittra, A hybrid finite-element finite-difference time-domain (FE/FDTD) technique for solving complex electromagnetic problems, IEEE Microw. Guide Wave Lett. 8 (2) (1998) 93–95, doi:10.1109/75.658652.

[11] A. Monorchio, A.R. Bretones, R. Mittra, G. Manara, R.G. Martin, A hybrid time-domain technique that combines the finite element, finite difference and method of moment techniques to solve complex electromagnetic problems, IEEE Trans. Antennas Propag. 52 (10) (2004) 2666–2674, doi:10.1109/TAP.2004.834431.

[12] M. Marrone, R. Mittra, A theoretical study of the stability criteria for hybridized FDTD algorithms for multiscale analysis, IEEE Trans. Antennas Propag. 52 (8) (2004) 2158–2167, doi:10.1109/TAP.2004.832332.

[13] M. Marrone, R. Mittra, A new stable hybrid three-dimensional generalized finite difference time domain algorithm for analyzing complex structures, IEEE Trans. Antennas Propag. 53 (5) (2005) 1729–1737, doi:10.1109/TAP.2005.846799.

[14] T. Rylander, A. Bondeson, Stable FEM–FDTD hybrid method for Maxwell's equations, Comput. Phys. Commun. 125 (1) (2000) 75–82, doi:10.1016/S0010-4655(99)00463-4.

[15] T. Rylander, A. Bondeson, Stability of explicit–implicit hybrid time-stepping schemes for Maxwell's equations, J. Comput. Phys. 179 (2) (2002) 426–438, doi:10.1006/jcph.2002.7063.

[16] T. Belytschko, R. Mullen, Stability of explicit–implicit mesh partitions in time integration, Int. J. Numer. Methods Eng. 12 (10) (1978) 1575–1586.

[17] J.-M. Jin, The Finite Element Method in Electromagnetics, second ed., John Wiley & Sons, New York, NY, 2002.

[18] W.C. Chew, J.-M. Jin, E. Michielssen, J. Song, Fast and Efficient Algorithms in Computational Electromagnetics, Artech House, Northwood, MA, 2001.

[19] J.-F. Lee, R. Lee, A. Cangellaris, Time-domain finite-element methods, IEEE Trans. Antennas Propag. 45 (3) (1997) 430–442, doi:10.1109/8.558658.
[20] T. Rylander, J.-M. Jin, Perfectly matched layer for the time domain finite element method, J. Comput. Phys. 200 (1) (2004) 238–250, doi:10.1016/j.jcp.2004.03.016.
[21] J.C. Nédélec, Mixed finite elements in R^3, Numer. Math. 35 (3) (1980) 315–341.
[22] P. Ingelström, A new set of H(curl)-conforming hierarchical basis functions for tetrahedral meshes, IEEE Trans. Microw. Theory Tech. 54 (1) (2006) 106–114.
[23] R. Remis, On the stability of the finite-difference time-domain method, J. Comput. Phys. 163 (1) (2000) 249–261, doi:10.1006/jcph.2000.6573.
[24] C. Schuster, A. Christ, W. Fichtner, Review of FDTD time-stepping schemes for efficient simulation of electric conductive media, Microw. Opt. Technol. Lett. 25 (1) (2000) 16–21.
[25] C.A. Balanis, Advanced Engineering Electromagnetics, John Wiley & Sons, New York, NY, 1989.
[26] N. Wang, Electromagnetic scattering from a dielectric-coated circular cylinder, IEEE Trans. Antennas Propag. 33 (9) (1985) 960–963.
[27] T. Halleröd, D. Ericsson, A. Bondeson, Shape and material optimization using gradient methods and the adjoint problem in time and frequency domain, COMPEL: Int. J. Comput. Maths Electr. Electron. Eng. 24 (3) (2005) 882–892, doi:10.1108/03321640510598201.
[28] G. Farin, From conics to NURBS: a tutorial and survey, IEEE Comput. Graph. Appl. 12 (5) (1992) 78–86, doi:10.1109/38.156017.
[29] A. Bondesson, T. Rylander, P. Ingelström, Computational Electromagnetics, Springer, New York, NY, 2005.
[30] J. Van Bladel, Field singularities at metal–dielectric wedges, IEEE Trans. Antennas Propag. 33 (4) (1985) 450–455.